In vitro studies of actin-microtubule coordination

Preciado Lopez, M.

2015

document version
Publisher's PDF, also known as Version of record

Chapter 4

Guidance of microtubule growth and organization by F-actin

In this chapter we study interactions between dynamic microtubules and actin filament bundles. We find that microtubule growth can be deflected by actin bundles through steric interactions in the absence of TipAct, or captured and guided via a zippering mechanism when TipAct is present. Microtubule zippering stems from TipAct's stable association with actin bundles, which recruits EB to the microtubule lattice in regions of actin-microtubule overlap. FRAP experiments reveal that both EB and TipAct's off rates are reduced in these regions, explaining the stability of the actin-microtubule connection. We further study the geometrical constraints on microtubule capture and guidance, and find that zippering via TipAct is more efficient than the deflection mechanism mediated by steric effects. Reducing the TipAct concentration shows that efficient microtubule guidance requires that the microtubule is coupled to the actin bundle all along its length. Finally, we demonstrate that TipAct allows sparse arrays of parallel F-actin bundles to globally dictate microtubule organization.

4.1 Introduction

Actin-microtubule coordination is essential for a variety of cellular processes, and in order to achieve this cells have evolved a variety of cross-talk mechanisms that are mediated by physical cross-linkers as well as signaling molecules [260]. One of the most studied instances of actin-microtubule coordination in cells consists of guidance of

microtubule growth by bundles of F-actin. This for example occurs in cell migration, where growing microtubules are targeted by the +TIP MACF along actin stress fibers towards focal adhesions (FAs) [279]. Microtubule targeting to FAs has been shown to control their disassembly [344, 364, 365], an essential requirement for cell motility [279]. FA disassembly is also regulated by the +TIP CLASP, which anchors the MACF-targeted microtubules at the cortex, in the vicinity of the FA site [87, 342]. These CLASP-anchored microtubules become tracks for the kinesin-1 dependent [343] delivery of factors involved both in endocytosis of FA components [470] and in extra-cellular matrix degradation [342].

Another important example of microtubule guidance by actin bundles occurs in extending neurons. In this situation, growing microtubules are targeted by the +TIP Shot along parallel actin bundles inside filopodia at the growth cone periphery [291, 354]. Local disruption of filopodial actin bundles or microtubules results in growth cones turning away from the site of drug application [370, 471]. It is thus widely accepted that cross-talk between filopodial actin bundles and microtubules controls the direction of growth cone extension [291, 354, 465]. However, the mechanisms by which filopodia selectively capture microtubules that invade the growth cone peripheral domain [291], and the ways by which these microtubules aid filopodia to steer a growth cone are hitherto unclear. When filopodial actin bundles are globally disrupted (without disturbing the dendritic actin meshwork that surrounds them), microtubules can indiscriminately invade the entire peripheral zone [373]. Although it has been speculated that filopodial roots acts as gates that limit the entrance into the peripheral domain [373], the mechanisms by which they would do so remain unresolved.

Even though in both examples outlined above the nature of the cross-linkers at play is known, our understanding of the ways by which they efficiently capture and guide microtubules is however incomplete. In both instances, the F-actin bundles are surrounded by a crowded environment, be it the cell interior (as in the case of stress fibers), or the lamellipodial F-actin network (as in the case of filopodial actin bundles). This raises a few questions: How do microtubules find their F-actin tracks? What is the dependency of microtubule capture and guidance on the cross-linker concentration? What are the mechanical and geometrical constraints for a microtubule to be deflected by an F-actin bundle?

Understanding the mechanisms that regulate efficient microtubule capture, as well as the geometrical and mechanical constraints that actin-microtubule cross-linkers have to offset in order to allow actin bundles to guide microtubule growth, could shed some

light onto these questions. To this end, we decided to study microtubule interactions with fascin-stabilized F-actin bundles, in the presence of EB3 and our model cross-linker TipAct. This chapter contains the results of these experiments.

4.2 TipAct and EB3 couple microtubule growth to F-actin bundles

In Chapter 3 we observed that our engineered actin-microtubule cross-linker, TipAct, can generate connections between microtubule growing ends and actin filaments (Fig. 3.9 a). This type of interactions occurred even at TipAct concentrations 100-fold lower than its dissociation constant from F-actin ($K_D \sim 5$ µM, Fig. 3.5). This observation reveals that TipAct's locally-enhanced concentration at microtubule tips (generated by EB3) can become sufficiently high to offset its low affinity for F-actin, thus allowing microtubules to bind F-actin. Furthermore, in these instances of actin-filament crosstalk with microtubule tips, we observed that the actin filament always co-aligned with the growing microtubule (Fig. 3.9 b). This can be explained by the 100-fold higher bending stiffness of microtubules ($EI_{MT} \sim 8$ pN µm^2 [89–91, 174]) compared to that of single actin filaments ($EI_{AF} \sim 0.04 - 0.07$ pN µm^2 [162, 174, 175, 472]).

Given these observations, we sought to test the hypothesis that bundled actin filaments, with an effectively higher bending stiffness [473, 474], would in turn act as guides for microtubule growth. To this end, we polymerized microtubules from GMPCPP-stabilized microtubule seeds, in the vicinity of bundles of F-actin stabilized by fascin, in the presence of 100 nM EB3 and 25-50 nM GFP-TipAct. The top panel in Figure 4.1 shows a schematic of theis assay.

In stark contrast to the microtubule-dependent interactions with single actin filaments (in otherwise identical experimental conditions), we observed that TipAct stably and independently associated with the F-actin bundles (Fig. 4.1, bottom panel). This could either be the result of the locally-increased F-actin concentration that results from bundling, or of TipAct having a different affinity for actin bundles *versus* single filaments. The latter effect has been reported of Dystrophin [475], a closely related protein to MACF (and hence TipAct), which contains a homologous tandem calponin-homology actin-binding domain [309]. In the case of TipAct an avidity effect could also be at play, since TipAct is a parallel homodimer, so that when bound to two actin filaments its

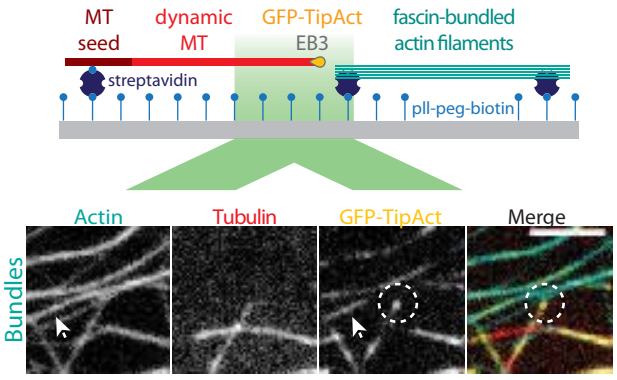

Figure 4.1: Experimental setup to study interactions between microtubules and F-actin bundles. Top, microtubules were polymerized from GMPCPP-stabilized seeds, in the presence of EB3, GFP-TipAct, and surface-bound F-actin filaments stabilized by fascin. Bottom, in these experiments TipAct localized both at microtubule tips (dashed circles) and at F-actin bundles (arrows). Scale bar, 5 µm. MT, microtubule.

effective off-rate could be reduced, and hence its affinity for actin bundles *versus* single filaments effectively increased.

We found that TipAct at F-actin bundles could also recruit mCherry-EB3 to these bundles (albeit weakly), even in the absence of microtubules (Fig. 4.2 a). In contrast, we never observed mCherry-EB3 recruitment to actin bundles when we replaced TipAct with a very similar protein construct (GFP-Tip) that lacked the actin-binding domain altogether (Fig. 4.2 b, [107]).

When we monitored microtubule growth in these assays, we observed that the enhanced TipAct (and hence EB3) localization at F-actin bundles was sufficient to force microtubule growth to proceed in tight association with the bundle (an effect we call *zippering*). Panel a in Figure 4.3 shows a montage of one such microtubule (whose plus-end is indicated by white arrowheads). Kymographs of *zippering* microtubules (Figure 4.3 b) revealed that the TipAct-dependent recruitment of mCherry-EB3 at F-actin bundles was further enhanced in regions of actin-microtubule overlap (Fig. 4.3 c). These observations suggest that actin-microtubule overlaps can have a stabilizing effect on the exchange dynamics of EB3 at microtubules and of TipAct at actin bundles. This effect is likely to enhance the strength of the actin-microtubule connection.

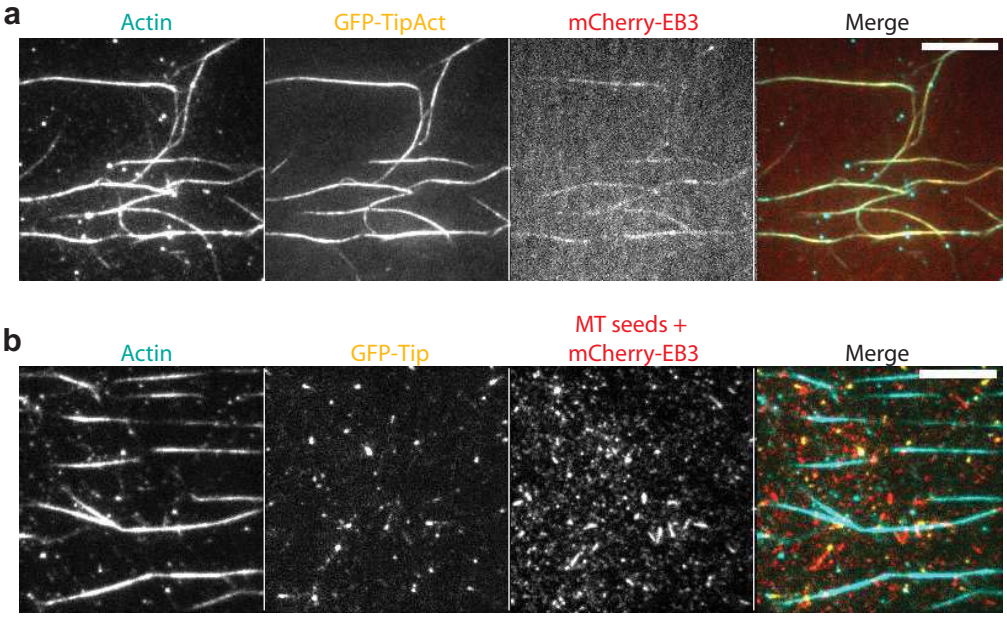

Figure 4.2: TipAct recruits EB3 to actin bundles, while a similar protein (GFP-Tip) lacking the actin-binding domain does not. (a) GFP-TipAct recruits mCherry-EB3 to fascin-stabilized F-actin bundles even in the absence of microtubules. (b) A protein construct similar to GFP-TipAct but which lacks the actin-binding domain does not localize to the F-actin bundles nor recruit mCherry-EB3 to these bundles. Scale bars, 10 µm. MT, microtubule.

4.3 EB3 and TipAct have reduced off-rates at actin-microtubule overlaps

In order to test whether the establishment of an actin-microtubule connection affects EB3 and TipAct's turnover rates, we performed high-temporal-resolution (33 ms/frame) fluorescence recovery after photobleaching (FRAP) experiments on free and actin-bound microtubule tips, as well as on free and microtubule-bound actin bundles, and tracked the fluorescence recovery of mCherry-EB3 and GFP-TipAct in all cases.

We found that both mCherry-EB3 and GPF-TipAct exchanged quickly at free microtubule growing ends (Fig. 4.4). A fit to the average fluorescence-recovery data (red curves in Fig. 4.4 b and c) to Equation (4.1) yielded an off-rate for mCherry-EB3 of $k_{off-EB:MTtip} \sim 1.8\ \mathrm{s}^{-1}$, and for GFP-TipAct of $k_{off-TA:MTtip} \sim 3.1\ \mathrm{s}^{-1}$, consistent with previously reported values of EB and +TIP exchange at microtubule growing ends [98, 100]. In the case of actin-bound microtubule tips, however, we found that fitting the fluorescence recovery data (blue curves in Fig. 4.4 b and c) with a single off-rate resulted in a poor fit to the data. We thus fit the recovery with two distinct off-rates (Eq. (4.2)),

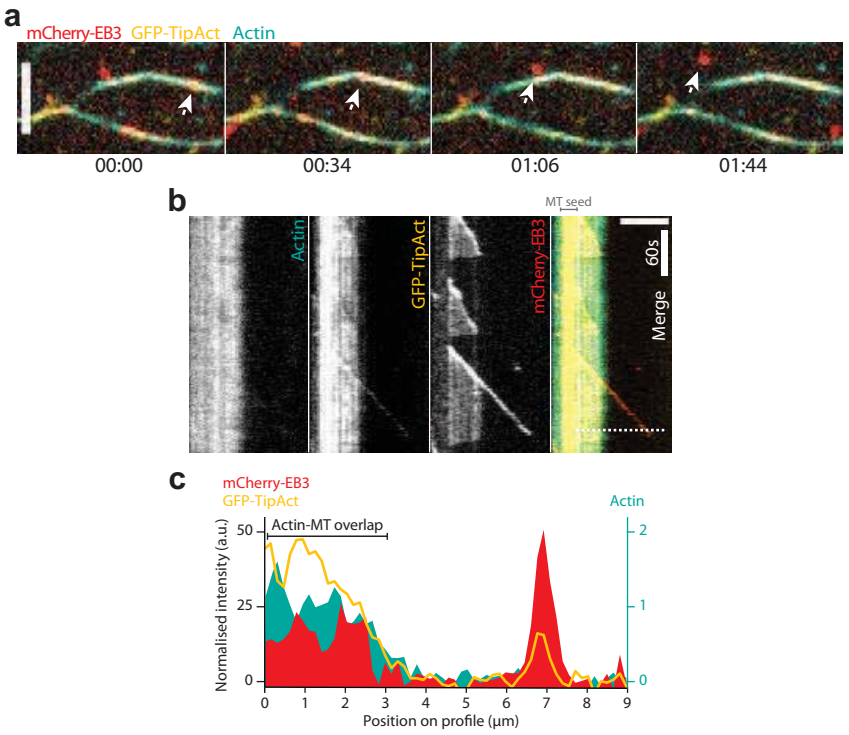

Figure 4.3: TipAct links microtubule growth to F-actin bundles. (a) Time series of an experiment as in Figure 4.1. Arrows show the plus-end of a microtubule that grows along an F-actin bundle with which it was initially co-aligned. (b) Kymograph of the microtubule indicated by arrows in (a). TipAct localizes at the F-actin bundle, and its fluorescence intensity increases in regions of actin-microtubule overlap. mCherry-EB3 localizes at microtubule tips, but also on the microtubule lattice in regions of actin-microtubule overlap. (c) Fluorescence intensity along the dashed line on the kymograph in (b), showing the accumulation of TipAct and EB3 at actin-microtubule overlaps. The GFP-TipAct and mCherry-EB3 intensities were normalized by their mean values at the free microtubule lattice, and the actin intensity by its mean value. Scale bars, 5 µm. Time: min:sec. MT, microtubule.

in order to separately account for the fraction of EB3 and TipAct not interacting with the actin bundle, and the fraction that was in contact with both microtubule tip and bundle. This revealed that the fraction of EB3 and TipAct linking the microtubule to the actin bundle exchanged three to five times slower ($k_{off-EB:MTtip-AB} = 0.8$ s^{-1}, and $k_{off-TA:MTtip-AB} = 0.7$ s^{-1}). It is worth noting that when we tried to fit the recovery data for free microtubules with two rates (Eq. (4.2)), we obtained the same value for both rates, confirming that in this situation there is only one exchanging species. As a direct consequence of the reduced off-rates of EB3 and TipAct at actin microtubule overlaps, we found that their plus-end intensity decayed to the steady-state microtubule lattice value two times slower compared to how it decayed at free microtubules. In all cases analyzed we verified that after bleaching the microtubule growth speeds remained the same (as can be observed in the example kymograph in Fig. 4.4 a). Thus, the

increased steady-state intensity of TipAct and EB3 at actin-microtubule tip overlaps can only be explained by effectively reduced off-rates. Panel d in Fig. 4.4 shows a summary of the measured rates in all cases, as obtained from fits to Equations (4.1) and (4.2).

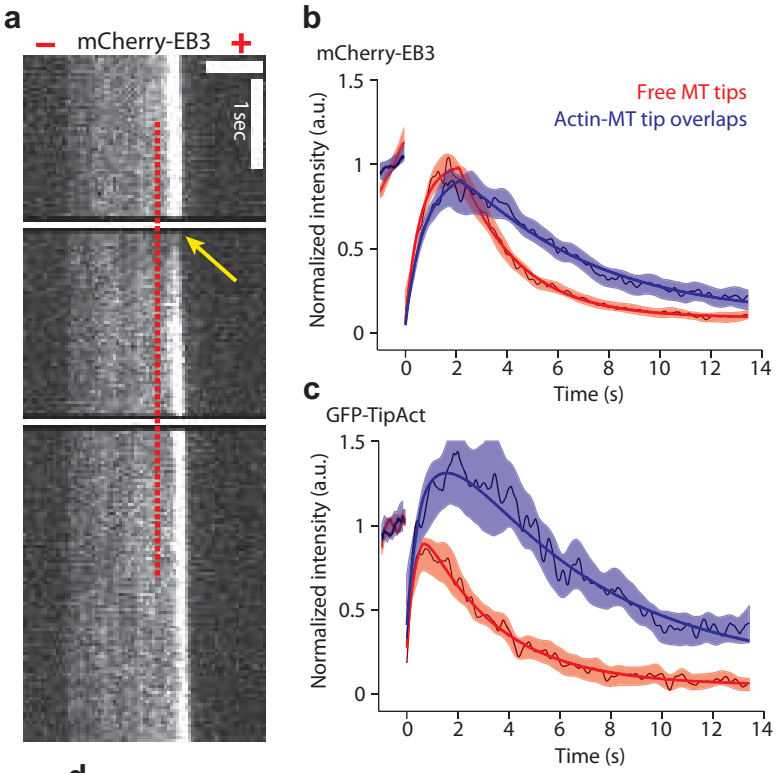

d

Protein	$k_{off\text{-}MTtip}$ (1/s)	$k_{decay\text{-}MTtip}$ (1/s)	$k_{off\text{-}MTtip}$ (1/s)	$k_{off\text{-}MTtip\text{-}AB}$ (1/s)	$k_{decay\text{-}MTtip\text{-}AB}$ (1/s)
mCherry-EB3	1.8	0.4	Fixed at 1.8	0.8	0.2
GFP-TipAct	3.1	0.3	Fixed at 3.1	0.7	0.2

Figure 4.4: FRAP experiments at microtubule plus-ends. (a) High temporal resolution (33 ms/frame) kymograph of microtubule growth showing the mCherry-EB3 intensity at the plus (+) end of a growing microtubule. The white horizontal line crossing the top of the kymograph indicates the bleaching frames, the yellow arrow the spot that was bleached, and the red-dashed line (shifted to the left of the mCherry-EB3 signal for ease of view), how the FRAP data was retrieved. Analysis of recovery curves for mCherry-EB3 (b) and GFP-TipAct (c) both at free (red) and actin-bound (blue) microtubule tips. The solid lines show the fits to Eq.(4.1) and Eq.(4.2), respectively. The thin colored lines and shaded areas show the average curves and SEM for n = 19 (free) and n = 13 (actin-bound) recovery profiles for mCherry-EB3, and n = 7 (free) and n = 6 (actin-bound) recovery profiles for GFP-TipAct respectively. Note that the maximum recovery intensity of GFP-TipAct at actin-bound microtubule tips reaches values larger than one due to the variable amount of GFP-TipAct that can localize to the F-actin bundles independently of microtubules. (d) Table showing the parameters obtained from the fits. Scale bar, 3 µm. MT, microtubule; AB, actin bundle.

Moreover, we found that GFP-TipAct stably associated with the F-actin bundles (both

free and microtubule bound), showing no recovery in either case within the timescale of observation ($k_{off-TA:AB} \leq 0.07$ s^{-1}, red and blue curves in Fig. 4.5 a and c). In contrast, mCherry-EB3 was dynamic in both cases (Fig. 4.5 b). In the case of free actin bundles (in the absence of microtubules), we fit the recovery data of EB3 (red curves in Fig. 4.5 b), with a single off-rate (Eq. (4.3)). This revealed that EB3 and TipAct do not form an irreversible complex in solution, as they dissociate in a timescale of seconds ($k_{off-EB:AB} = 0.3$ s^{-1}, Eq. (4.3)). Similar to the analysis at microtubule tips, we fit the recovery of EB3 at actin-bound microtubules (blue curves in Fig. 4.5 b), with two recovery rates (Eq. (4.4)), to separately account for the fraction of EB3 in contact with both microtubule and actin bundle, and the fraction of EB3 only in contact with the microtubule. The fraction of EB3 that only interacted with the microtubule lattice exchanged fast ($k_{off-EB:MT} = 2.2$ s^{-1}), consistent with previous reports [98]. In contrast, when bound to both microtubule lattice and actin bundle, EB3 exchanged 20 times slower ($k_{off-EB:AB-MT} \sim 0.1$ s^{-1}). Panel d in Fig. 4.5 shows a summary of the measured rates in all cases, which were obtained from fits to Equations (4.3) and (4.4).

The schematics in Figure 4.6 help us interpret these results: First, at free microtubule tips the exchange rate of EB3 and TipAct is dominated by the off-rate of EB3, which is approximately six-fold higher ($k_{off-EB:MTtip} = 1.8$ s^{-1}) than the dissociation rate of EB3 and TipAct ($k_{off-EB:AB} = 0.3$ s^{-1}). Second, TipAct's stable localization at actin bundles ($k_{off-TA:AB} < 0.07$ s^{-1}), results in the fraction of EB3s in contact with both microtubule and bundle to exchange five to twenty times slower ($k_{off-EB:MTtip-AB} = 0.8$ s^{-1}, $k_{off-EB:MT-AB} = 0.1$ s^{-1}) than they normally do on free microtubules. The FRAP experiments thus revealed two important things: first, that EB3 and TipAct do not form an irreversible complex in solution; and second, that the way by which EB3 and TipAct mediate stable linkages between actin bundles and microtubules stems from TipAct's stable localization at the actin bundles, which in turn leads to a reduced off-rate of EB3 in regions of actin-microtubule overlap.

4.4 Actin bundles capture and redirect growing microtubules

In the previous section we observed that TipAct's stable association with F-actin bundles has a stabilizing effect on EB3 in regions of actin-microtubule overlap. This helps explain how TipAct and EB3 efficiently couple microtubule growth to actin bundles (Fig. 4.3).

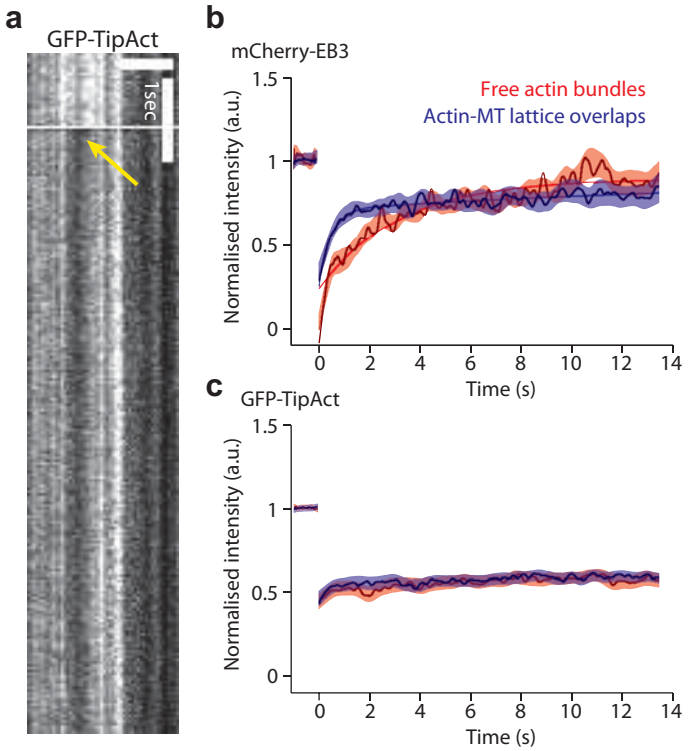

d

Protein	$k_{off\text{-}AB}$ (1/s)	$k_{off\text{-}MTlatt}$ (1/s)	$k_{off\text{-}AB\text{-}MTlatt}$ (1/s)
mCherry-EB3	0.3	2.2	0.1

Figure 4.5: FRAP experiments at F-actin bundles. (a) High temporal resolution (33 ms/frame) kymograph of GFP-TipAct on an actin bundle. The white horizontal line crossing the top of the kymograph indicates the bleaching frames and the yellow arrow the spot that was bleached. Analysis of recovery curves for mCherry-EB3 (b) and GFP-TipAct (c) both at free (red curves) and microtubule-bound (blue curves) actin bundles. The solid lines in (b) show the fits to Eq.(4.3) and Eq.(4.4), respectively. We did not fit the GFP-TipAct data since it showed no recovery in the timescale of observation. The thin colored lines and shaded areas show the average curves and SEM for n = 12 (free) and n = 17 (actin-MT overlaps) recovery profiles for mCherry-EB3, and n = 19 (free) and n = 19 (actin-MT overlaps) recovery profiles for GFP-TipAct, respectively. (d) Table showing the parameters obtained from the fits. Scale bar, 3 µm. MT, microtubule; AB, actin bundle.

However, as mentioned in the introduction, another key unanswered question in the study of actin-microtubule interactions, is what are the geometrical and mechanical constraints that cross-linkers, such as MACF and Shot, have to overcome in order to capture and redirect microtubule growth. We thus set out to test if the actin-to-microtubule linkages mediated by TipAct and EB3 could be sufficiently strong to offset the mechanical energy cost involved in deforming a microtubule that does not start-off parallel to the F-actin bundle.

To this end, we polymerized microtubules with 100 nM EB3, in the presence and absence

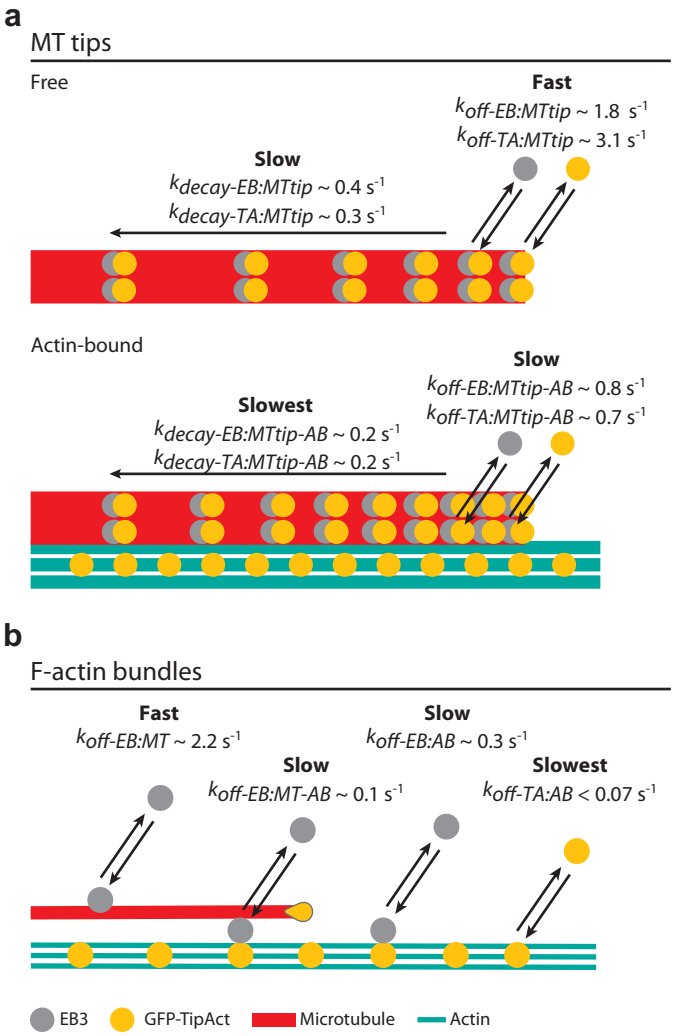

Figure 4.6: Schematics to interpret the FRAP experiments. (a) Top, at free microtubule tips, EB3 and TipAct exchange in less than 1 sec, while their intensity decays to the steady-state lattice value in $\sim 2-3$ sec. Bottom, at actin-bound microtubule tips, both EB3 and TipAct exchange more slowly, in $\sim 1-2$ sec. This results in a slower transition to the steady-state lattice intensity, in ~ 5 sec. (b) TipAct is basically *fixed* at the F-actin bundles, and recruits EB3, which exchanges in ~ 3 sec, even in the absence of microtubules. At actin-microtubule overlaps, the fraction of EB3 in contact with both the microtubule and the actin bundle exchanges even slower, in ~ 10 sec. In contrast, the fraction of EB3 only in contact with the microtubule exchanges in less than 1 sec.

of 50 nM GFP-TipAct, in the vicinity of F-actin bundles stabilized by fascin (in an assay as in Fig. 4.1). As in the previous assays, we included 0.1 % (v/v) methyl-cellulose to confine microtubule and actin-bundle out-of-plane fluctuations, allowing us to have a quasi two-dimensional system. In the presence of TipAct, microtubules were often captured by the F-actin bundles, which furthermore were able to deflect the microtubule tip so that all subsequent growth *zippered* along the bundle (Fig. 4.7 a). For microtubules that encountered the actin bundles at high angles, this resulted in sharp bends of the microtubule lattice near the point of first contact. This observation is reminiscent of recent studies of microtubule guidance by actin stress-fibers in cells cultured on adhesive micro-patterns, in which microtubules were also observed to sustain sharp deformations [368]. Likely due to the quasi two-dimensional geometry of our assays, we found that in the absence of TipAct, microtubules could also be guided by the actin bundles. However, in contrast with the sharp deformations observed in the presence of TipAct, these microtubules bent smoothly all along their length (Fig. 4.7 b). In this situation, the microtubule tip was likely *deflected* by repeated collisions with the F-actin bundle. This type of steric interactions are typically used by plant cells to organize the cortical microtubule arrays [295].

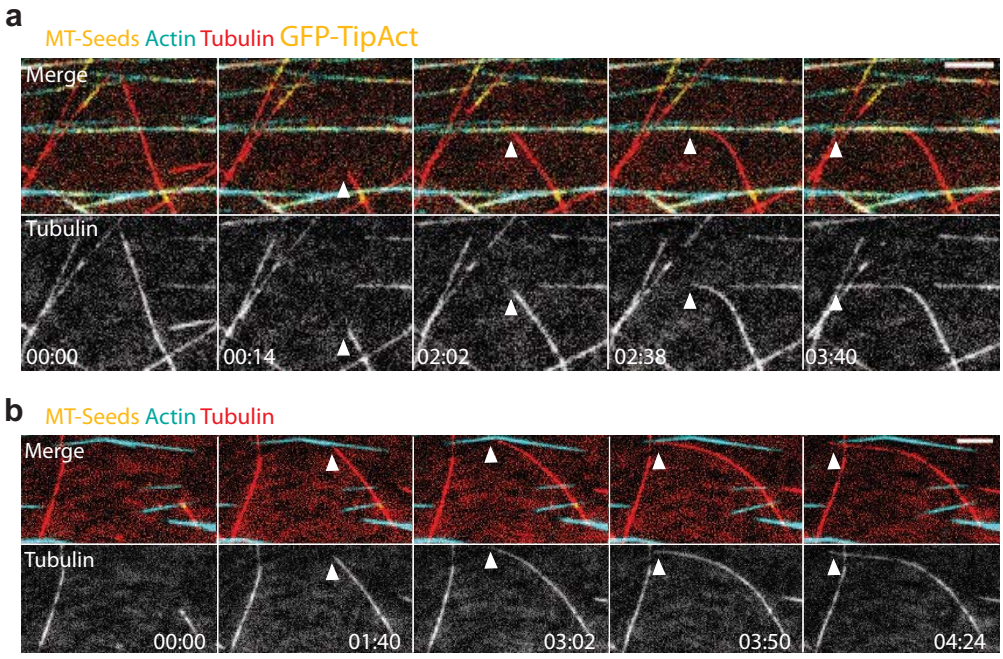

Figure 4.7: Two different mechanisms of microtubule guidance by F-actin bundles. (a) Time series of a microtubule grown with GFP-TipAct that is captured and then zippers along an F-actin bundle as it continues to grow. (b) Time series of a microtubule grown without GFP-TipAct, whose tip is mechanically deflected by an F-actin bundle as it continues to grow. In (a) and (b) the plus-ends of the microtubules are indicated by arrowheads. Scale bars, 10 µm. Time, min:sec. MT, microtubule.

Microtubules have an approximately 100-fold higher-bending stiffness ($EI_{MT} \sim 8$ pN µm^2 [89–91, 174]) compared to single actin filaments ($EI_{AF} \sim 0.04 - 0.07$ pN µm^2 [162, 174, 175, 472]), which indicates that the mechanical bending stiffness provided by actin-bundling can become comparable to that of a microtubule, so that the microtubule is deformed by the actin bundle and not the other way around. *In vitro* studies on fascin-bundled actin filaments have shown that the bending stiffness of these bundles increases both with the molar ratio of fascin to G-actin, and with the number of actin filaments in the bundle [473, 474]. In our assays, we kept the fascin to G-actin molar ratio between 1:2 and 1:5, which would correspond to an actin-bundle bending stiffness, EI_{AB}, in the range of $2 - 30$ pN µm^2 if 6-30 actin filaments were present in the bundles [473]. Although we did not measure the number of actin filaments independently, this range of values is already comparable to the bending rigidity of a microtubule. It is worth noting that in addition to the mechanical stabilization that stems from bundling F-actin, the actin bundles were also anchored to the coverslip surface, which acts to reduce their mobility and further enhance their *effective* bending rigidity.

These results show that microtubule growth can be captured and redirected by actin bundles via *zippering* with, and *deflection* without, TipAct. Furthermore, that capture and guidance can lead to mechanical deflection of the microtubule lattice (either locally with TipAct, or all along its length without it). Next, we wanted to understand under what conditions capture and guidance would occur in both cases. To this end, we monitored microtubule tip encounters with actin bundles, and characterized the outcome of these interactions into three categories, in a similar fashion as how interactions between plant cortical microtubules have been analyzed [295]: catastrophe, cross-over, and zippering or deflection, with or without TipAct respectively (Fig. 4.8 a). We studied the probability of these outcomes as a function of microtubule length L_{MT}, and intersection angle θ, between the microtubule and the F-actin bundle at the point of first contact (Fig. 4.8 a).

As discussed above, without TipAct, microtubules were deflected by collisions of their growing tip with the actin bundles. This effect was dominant at shallow angles ($< 5°$), occurred approximately 50% of the cases for intermediate angles ($5 - 25°$), and was rare at encounter angles $> 25°$ (Fig. 4.8 b). In contrast, with TipAct, the probability of zippering dominated the outcomes up to encounter angles of $\sim 25°$ (Fig. 4.8 c). Furthermore, capture of microtubule ends by TipAct reduced the probability of microtubule catastrophe induced by collisions [93] at small encounter angles (Fig. 4.8 c), and made capture insensitive to microtubule length (Fig. 4.8 d). This is in contrast to the deflection mechanism without TipAct, which was dependent (albeit weakly) on microtubule length

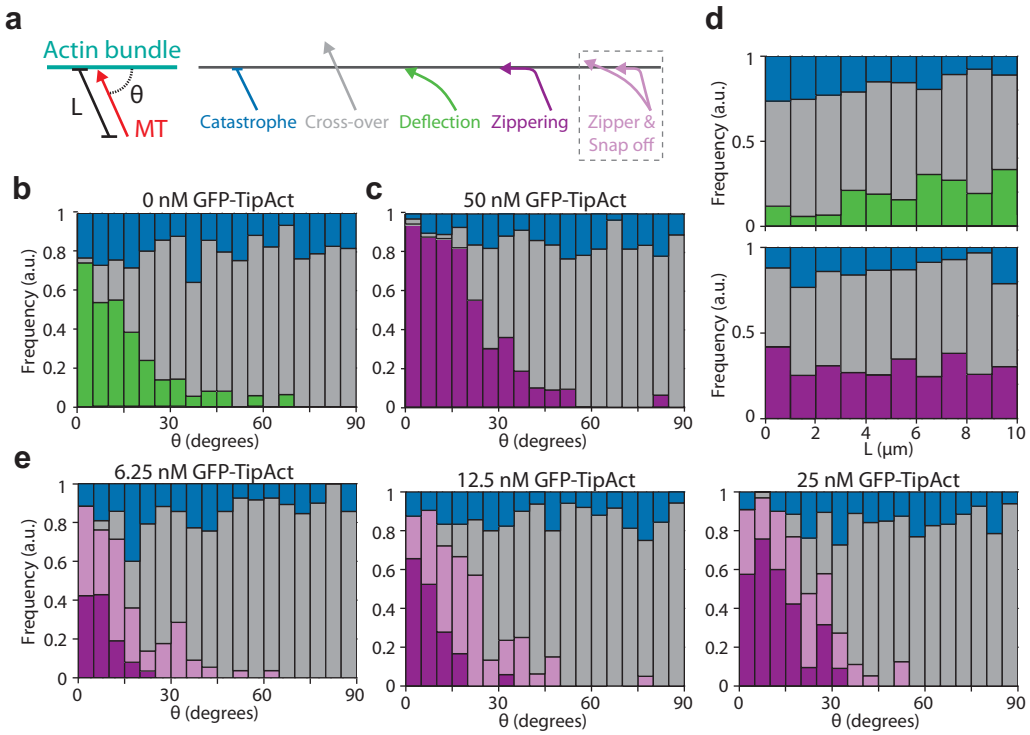

Figure 4.8: Probability of microtubule guidance by deflection *versus* zippering. (a) Classification of the interaction outcomes between growing microtubules and F-actin bundles, and how the intersection angle θ and microtubule length L were defined. Probability of each interaction outcome as a function of θ, with (c) or without (b), 50 nM GFP-TipAct. (d) Probability of each interaction outcome as a function of L, with (bottom) or without (top) 50 nM GFP-TipAct. (e) Probability of each interaction outcome as a function of θ for variable GFP-TipAct concentrations. For each of the following conditions: 0, 6.25, 12.5, 25 and 50 nM GFP-TipAct, n = 708, 459, 421, 443 and 914 interactions were analyzed respectively. The data in (b) and (c) was obtained from n = 9 and 6 experiments, respectively.

(Fig. 4.8 d), since in this case catastrophes occurred more often, especially for short microtubules. These observations highlight the mechanical component of microtubule capture and deflection, as well as the probability that during growth a microtubule is very likely to *miss* the F-actin track (especially at high angles), through spatial fluctuations of the microtubule tip in the z-direction. We anticipate that in the crowded, three-dimensional environment of the cell, capture and guidance of microtubules by actin bundles via steric effects is likely to be even less common than in the quasi two-dimensional geometry of our assays.

4.4.1 Dependency of microtubule guidance on TipAct concentration

In order to test the contributions of microtubule tip and lattice to the capture and guidance mechanism of TipAct, we performed further experiments with decreasing amounts of TipAct while keeping the EB3 concentration constant. In these situations we found that a new interaction outcome had to be added to the classification, namely *zipper & snap-off* (Fig. 4.8 a), since with decreasing TipAct concentration an increasing portion of microtubules eventually *snapped-off* the F-actin track. This occurred at both high and shallow encounter angles (Fig. 4.9 a and b), although the angular dependency of initial capture remained approximately the same (Fig. 4.8 e). Furthermore, at the lowest concentration of TipAct used (i.e. 6.25 nM), we found that a large fraction of microtubules interacted with the actin bundles solely via their growing tips (Fig. 4.9 c), resulting in a guidance mechanism nearly indistinguishable from that of mechanical deflection (Fig. 4.7 b), when TipAct was fully absent.

Put together, these observations indicate that the energy required to redirect a microtubule can be efficiently overcome when a sufficient amount of cross-linkers is present. Although guidance of microtubule growth can occur by purely steric effects (Fig. 4.7 b), in these situations the microtubule is forced to traverse the space next to the bundle. We speculate that in the crowded, three-dimensional geometry of the cell interior this mechanism of microtubule guidance is unlikely to be efficient, as microtubules will be very likely to lose their F-actin tracks. Although the microtubule tip plays a key role in the initial capture event (since we never observed a microtubule aligning with an actin bundle that it had initially crossed-over), decreasing the amount of TipAct revealed that when the density of cross-linkers is not high enough, captured microtubules are more susceptible to detach from the actin bundles. Therefore, the presence of a sufficiently-high density of cross-linkers, at the actin-microtubule overlap, is a requirement for microtubule growth to proceed in tight association with F-actin. This effect could act to protect the microtubule tip from the many obstacles ubiquitous to the crowded interior of the cell, and is likely to be one of the most efficient ways to reliably target microtubule growth to particular sites in the cell; such as focal adhesions at the end of actin stress-fibrers [279, 344, 364], or to the ends of filopodia [291, 354, 465].

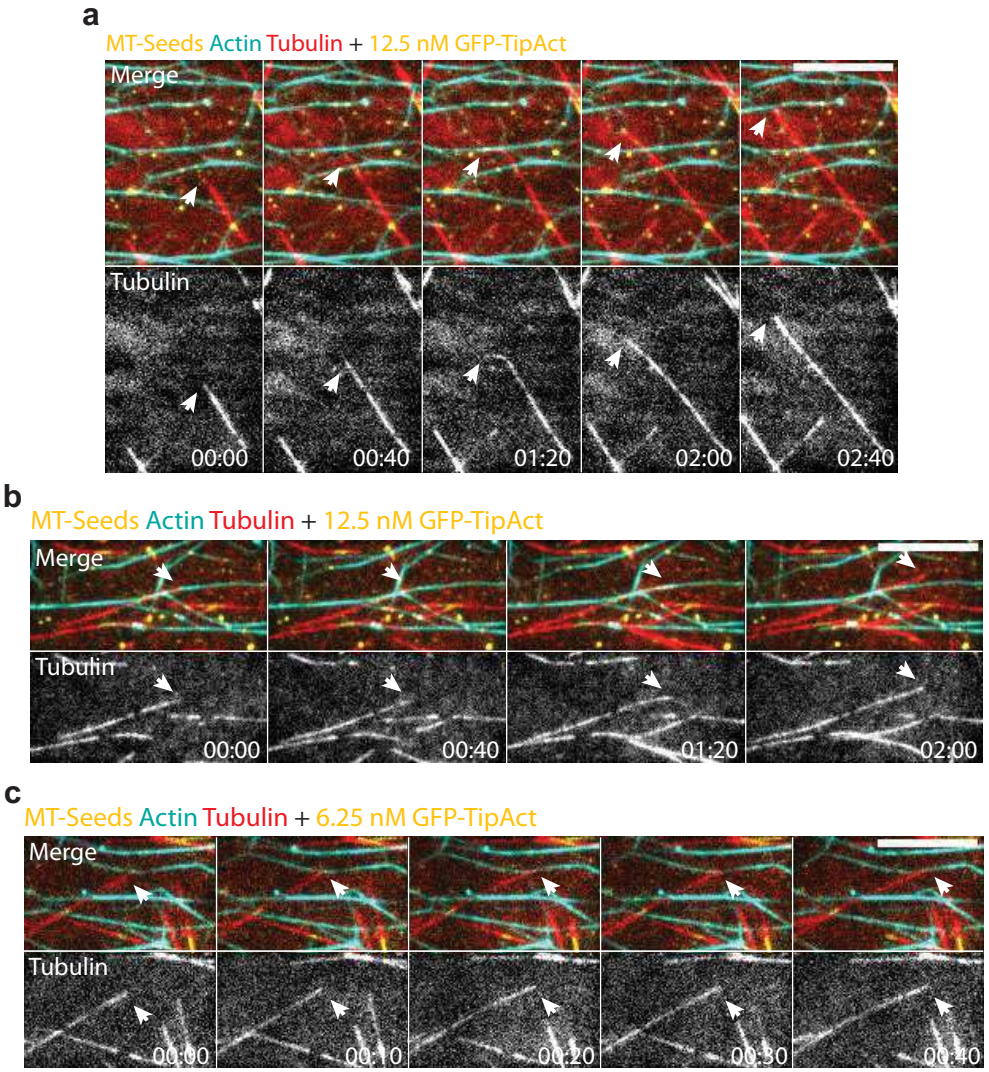

Figure 4.9: Dependency of microtubule guidance on TipAct concentration. Time series of microtubules grown with 12.5 nM GFP-TipAct, which encounter an actin bundle both at high $\sim 62°$ (a), and shallow $\sim 17°$ (b) angles, both of which begin to zipper but eventually snap-off. (c) Time series of a microtubule grown with 6.25 nM GFP-TipAct which follows the F-actin bundle only with its growing tip. In (a), (b) and (c) the plus-ends of the microtubules are indicated by arrowheads. Scale bars, 10 µm. Time, min:sec. MT, microtubule

4.5 Ordered arrays of F-actin bundles can globally dictate microtubule organization

It has been shown that actin-microtubule cross-linking +TIPs such as MACF, CLASP and APC, are necessary to establish parallel arrays of microtubules perpendicular to the cell edge [123, 279, 332, 335, 340]. Organizing microtubules in such a way facilitates the polarized transport of vesicles and proteins to the leading edge of motile cells, and to maintain directional cell migration [476]. Given that both mechanical effects and physical cross-linking by EB3 and TipAct allow F-actin bundles to guide microtubule growth (Fig. 4.7), albeit with different efficiency (Fig. 4.8), we wondered to what extent these effects would allow a well-defined F-actin bundle architecture to globally dictate microtubule organization. To this end, we generated sparse arrays of parallel F-actin bundles stabilized by fascin, interspersed with randomly oriented GMPCPP-stabilized microtubule seeds. As in the previous assays, we polymerized microtubules in quasi two-dimensional confinement by the addition of 0.1 % (v/v) methyl-cellulose, in the presence of 100 nM EB3, with or without 50 nM GFP-TipAct. Under these conditions, the average microtubule length ($\langle L_{MT} \rangle$) continuously increased (Fig. 4.16), which allowed us to monitor the temporal evolution of actin-microtubule co-alignment as a function of $\langle L_{MT} \rangle$.

The left-most panels in Figure 4.10 a show two examples of the F-actin bundle arrays we could generate, and the second and third panels the initial ($t \sim 5$ min) and final ($t \sim 1$ hr) arrays of dynamic microtubules that ensued in the presence (top), or absence (bottom), of TipAct. In both cases, at the early stages of the experiment the microtubules already adopted an average orientation angle that weakly corresponded to that of the underlying F-actin bundle array. In later stages, however, while the microtubules grown in the presence of TipAct maintained their alignment with the actin bundles, a large number of microtubules grown in the absence of TipAct were oriented at random angles relative to the mean actin bundle orientation. Plots of the distribution of microtubule orientation angle (θ_{MT}) over time, revealed that both with and without TipAct, the microtubule arrays became increasingly aligned about the mean F-actin angle ($\langle \theta_{ACTIN} \rangle$, Fig. 4.10 b). However, and in agreement with the fluorescence images shown in Figure 4.10 a, with TipAct the final peak of the distribution of θ_{MT} was narrower and more intense.

To better quantify the difference in organization efficiency that stems from physical cross-linking versus mechanical deflection, we quantified the degree of microtubule alignment

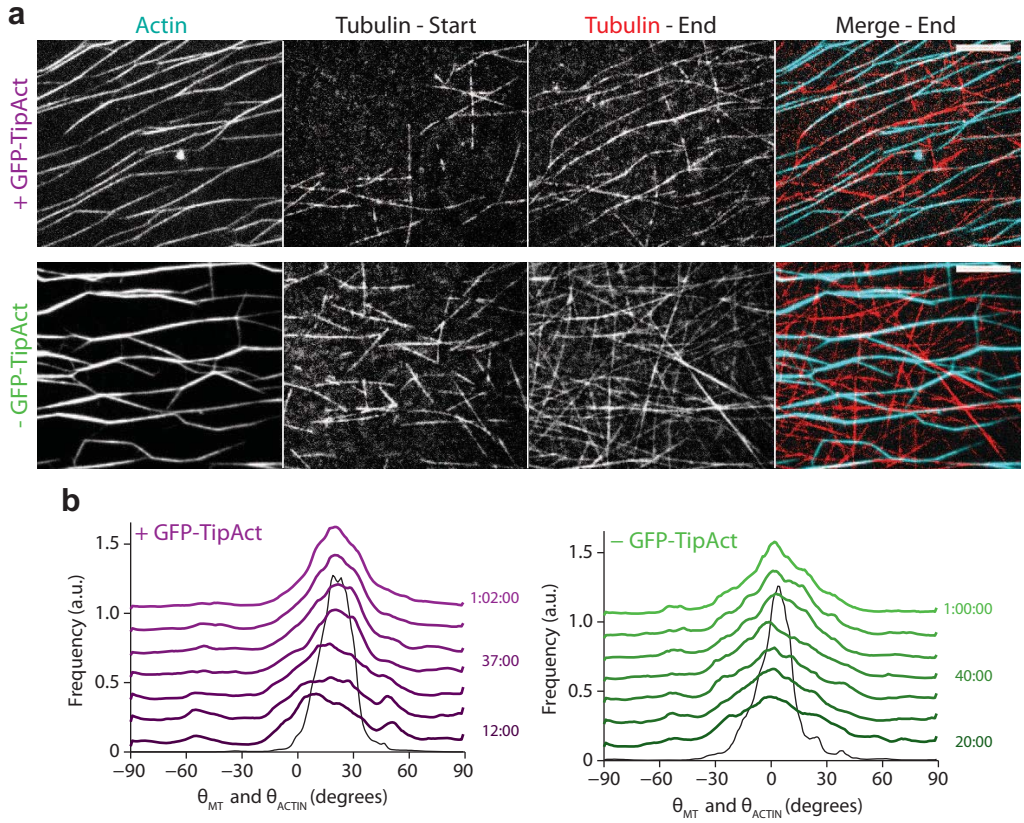

Figure 4.10: Linear arrays of F-actin bundles globally dictate microtubule organization. (a) Early ($t \sim 5$ min) and late ($t \sim 1$ hr) time points of microtubule growth within linear arrays of fascin-stabilized actin bundles with (top), and without (bottom), 50 nM GFP-TipAct. (b) Evolution of the distributions of microtubule orientation angle θ_{MT}, for the experiments in (a). Color gradients indicate the time evolution of the distribution. For ease of view, each curve is shifted 0.17 a.u. relative to the previous one. The black curves show the time-averaged distribution of F-actin bundle orientation angle $\langle\theta_{ACTIN}\rangle$.

with several such F-actin bundle arrays. To this end, we made use of an order parameter (Eq. (4.6)), a unit-less quantity typically used to estimate the strength of alignment of filamentous structures (independent of polarity), relative to a reference angle [477]. Given the dependency of microtubule capture and guidance on microtubule length (Fig. 4.8 e), we analyzed microtubule alignment as a function of $\langle L_{MT}\rangle$, which we estimated from the fraction of the field of view covered by microtubules (Fig. 4.17).

In the presence of TipAct, microtubule alignment monotonically increased with $\langle L_{MT}\rangle$ (purple data points in Fig. 4.11 a). However, in the absence of TipAct we found that, while microtubule alignment increased linearly for $\langle L_{MT}\rangle \leq 19$ µm, for higher values of $\langle L_{MT}\rangle$ the microtubule alignment showed no discernible trend (green data points in Fig. 4.11 a). In addition to this, we measured the degree of overlap between the microtubules and the F-actin bundles. As expected, through the *zippering* mechanism,

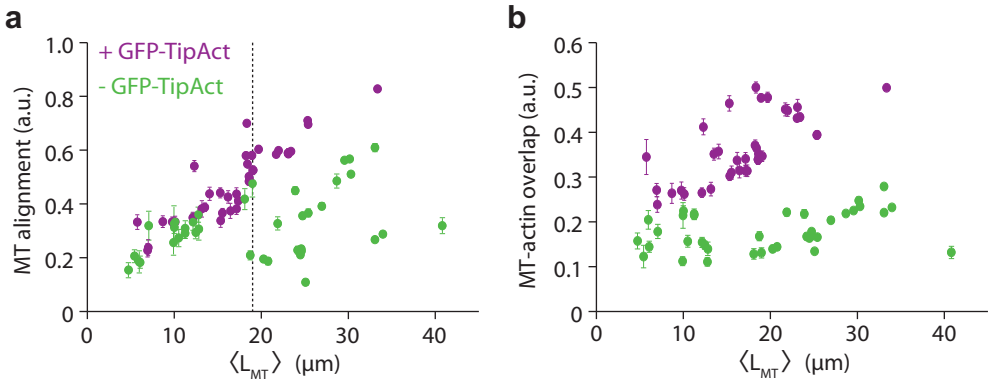

Figure 4.11: Microtubule alignment increases with $\langle L_{MT} \rangle$. Evolution of microtubule alignment (a), and actin-microtubule overlap (b), as functions of the average microtubule length, $\langle L_{MT} \rangle$. Error bars are STD. The gray-dashed line at $\langle L_{MT} \rangle = 19$ µm in (a) indicates where the trends between the zippering (with TipAct) and deflection (without TipAct) guidance mechanisms start to diverge. Data was obtained from n = 6 and 9 experiments with and without 50 nM GFP-TipAct, respectively. MT, microtubule.

microtubules grown in the presence of TipAct showed an increasing degree of overlap with the F-actin bundles with increasing $\langle L_{MT} \rangle$ (purple data points in Fig. 4.11 b). In contrast, microtubules grown without TipAct maintained an approximately constant degree of overlap with the bundles (green data points in Fig. 4.11 b), independent of $\langle L_{MT} \rangle$, which mainly consisted of random cross-overs (Fig. 4.10 a, bottom).

We then built the average distribution of microtubule orientation angles (θ_{MT}), relative to the corresponding mean actin orientation ($\langle \theta_{ACTIN} \rangle$) across experiments, and fit these average curves to a Gaussian (Eq. (4.5), Fig. 4.12). The value of μ represents the difference in mean orientation between the microtubules and the actin bundle array, i.e. $\langle \theta_{ACTIN} \rangle - \theta_{MT}$, which can be understood as the *centering efficiency*, the smaller its value, the better the actin-microtubule co-alignment. On the other hand, the value of σ can be interpreted as the *focusing efficiency*, that is, the smaller its value, the more globally the microtubule array has been aligned by the underlying actin bundle array. These plots thus reveal that microtubule *zippering* via EB3 and TipAct always results in better microtubule co-alignment with the actin-bundle arrays. This was the case both for short microtubules ($\langle L_{MT} \rangle \leq 19$ µm, Fig. 4.12 a), and even more strongly for long microtubules ($\langle L_{MT} \rangle > 19$ µm, Fig. 4.12 b). These observations confirm that even though mechanical deflection via steric interactions can under certain conditions direct microtubule growth (Fig. 4.7 b), the lack of anchors to the F-actin bundles makes microtubules susceptible to lose their tracks. Thus, in conditions where the F-actin bundles are sparse, the activity of cross-linkers is definitely required to dictate global actin-microtubule co-alignment.

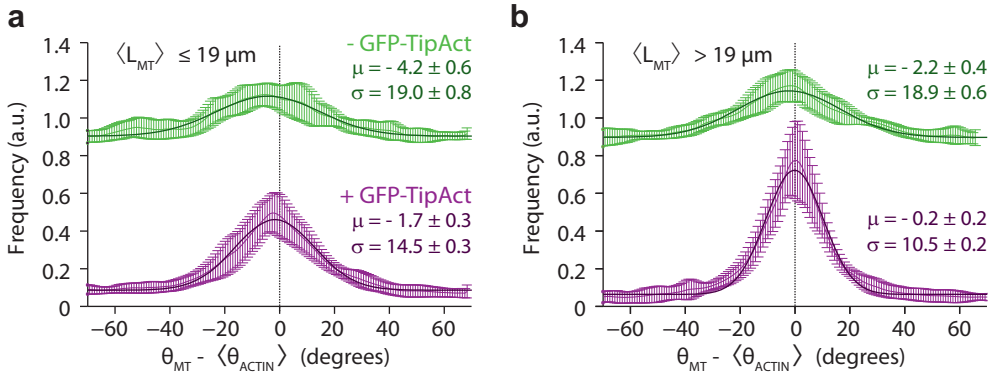

Figure 4.12: Average histograms of actin-microtubule co-alignment. Average histograms of the difference between microtubule and mean F-actin orientation angle, i.e. $\langle\theta_{ACTIN}\rangle - \theta_{MT}$, for short $\langle L_{MT}\rangle \leq 19$ (a), and long $\langle L_{MT}\rangle > 19$ (b), microtubules (as defined in Figure 4.11 a). Error bars are STD. Dark green and purple lines and insets show the fits to Eq. (4.5). Data and fits without GFP-TipAct were shifted up 0.8 a.u. for ease of view. Data is the average of n = 6 and 9 experiments, comprising 17 and 9 histograms for long microtubules, and 18 and 11 histograms for short microtubules, with and without 50 nM GFP-TipAct, respectively.

4.5.1 Actin bundle density tunes actin-microtubule coordination

In the previous section we found that actin-microtubule cross-linking via EB3 and TipAct is required to allow sparse arrays of parallel F-actin bundles to globally organize an otherwise random microtubule array. Furthermore, we found that in the absence of TipAct, microtubules are increasingly susceptible to lose track of the F-actin bundle as they grow. This observation suggests that the spatial density of F-actin bundles plays an important factor in regulating actin-microtubule organization. In fact, for all the experiments outlined above, we were careful to compare F-actin bundle arrays in which the number of bundles and their spacing was approximately the same. However, the experimental protocol to create such arrays often yielded variable F-actin bundle densities, which allowed us to study this effect.

The left panels in Figure 4.13 a show three examples of F-actin bundle arrays with different density, the middle panels show the resulting microtubule organization ∼1 hr after the start of the experiment, and the right-most panels show the merged images. With increasing F-actin bundle density, even in the absence of TipAct, the microtubules can better co-align with the underlying F-actin bundle architecture. The histograms in Fig. 4.13 b show that even though the original organization of the microtubules was approximately random, with time, the microtubules adopted the underlying F-actin

organization, with the highest degree of co-alignment with the densest F-actin bundle array.

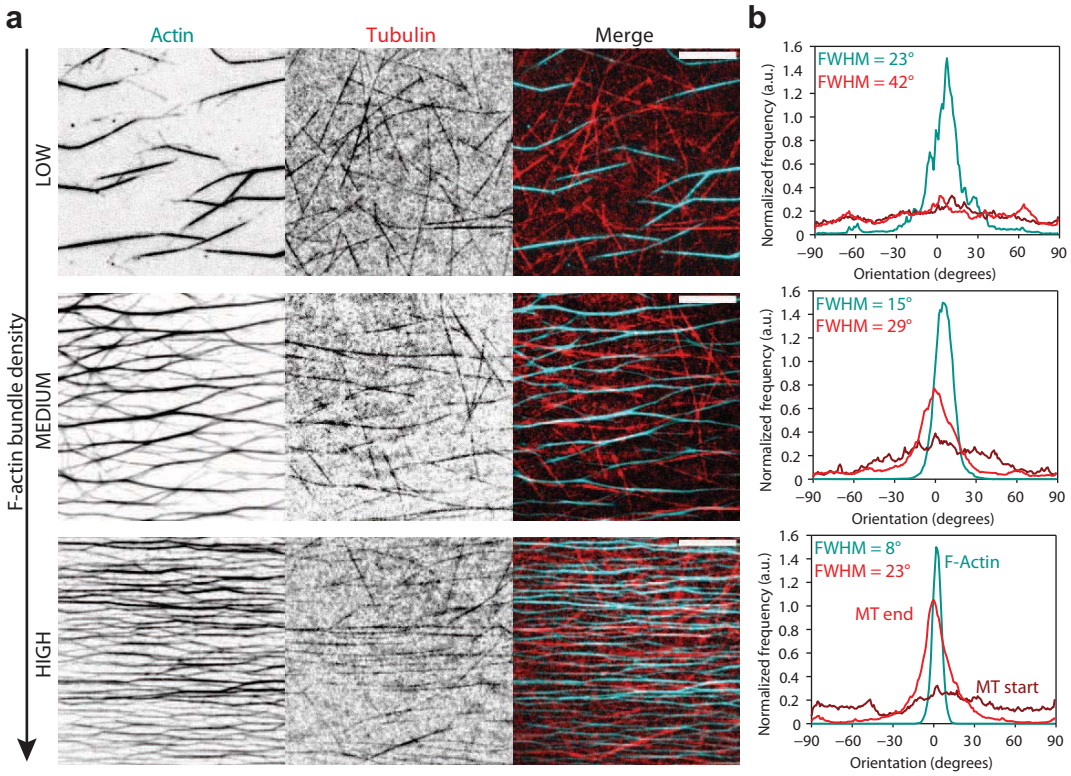

Figure 4.13: Increasing the F-actin bundle density leads to better actin-microtubule co-alignment through steric interactions. (a) Resulting microtubule organization after ∼1 hr of growth within the corresponding F-actin bundle array shown in the left panels. (b) Normalized histograms of F-actin bundle and microtubule orientation for the examples in (a), with the same color-coding. The dark- and light-red curves show the initial and final distributions of microtubule orientation. The full-width at half maximum (FWHM, obtained from fits to Eq.(4.5)), is shown in the insets, both for the actin bundles and the final microtubule arrays. Scale bars: 10 µm. MT, microtubule.

This result demonstrates that besides the action of cross-linkers, the role of steric interactions in directing actin-microtubule organization is key. And further suggests that in some contexts, cells may rely on specific F-actin architectures to direct microtubule growth, even in the absence of cross-linkers.

4.6 Discussion

In this chapter we have demonstrated the ability of F-actin bundles to capture and redirect microtubule growth. Furthermore, we have shown how microtubule capture

and guidance depends on the concentration of cross-linkers, as well as the encounter angle and length of the microtubule when it meets the actin bundle. In the presence of TipAct, guidance occurred by *zippering* of the microtubule onto the F-actin bundle, and in its absence, through steric interactions between the microtubule tip and the bundle.

Furthermore, we showed that even though TipAct is a weak actin-filament binder, with a dissociation constant for F-actin in the order of 5 µM, it nonetheless displays a strong localization at fascin-stabilized actin bundles. This could be the result of an avidity effect, given that TipAct is a parallel homodimer, which would imply that when its two actin-binding domains are bound to F-actin its effective off-rate is reduced. Similar observations have been reported of Dystrophin, a closely related protein to MACF (hence TipAct) which also contains a tandem calponin-homology (CH) actin-binding domain [475]. However, dystrophin molecules are monomeric [478], which suggests that a preference for F-actin bundles *versus* single filaments may be a property of tandem CH actin-binding domains. This could be tested, for instance, by generating monomeric versions of TipAct. Given that TipAct's actin-binding domain is identical to that of MACF, our observations could help explain MACF and Shot's predominant role as actin-microtubule cross-linkers on F-actin bundles (i.e. stress-fibers and filopodia), rather than at dendritic or cortical F-actin networks, in living cells [122, 123, 125, 352, 354, 369, 465].

TipAct's strong localization at fascin-stabilized actin bundles was sufficient to recruit EB3 to the bundles as well, even in the absence of microtubules. FRAP experiments further revealed that TipAct remains practically fixed at the bundles on the timescale of microtubule growth, as well as on the timescale of TipAct and EB3 exchange at microtubule tips. This results in enhanced steady-state concentrations of both EB3 and TipAct at actin-microtubule overlaps, which explains how they can mediate stable actin-microtubule connections. This observation could also help explain the reported enhancement of MACF, Shot and EB1 localization along microtubules in actin-rich regions in cells [123, 125]. Given that full-length MACF and Shot molecules also contain a microtubule-lattice binding domain (Fig. 3.1), we speculate that in *in vivo* this mechanism could act in synergy with (or even as a preceding step to) the establishment of actin-microtubule linkages mediated by MACF and Shot's microtubule lattice-binding domain [309, 354], which is the most heavily regulated domain of these molecules [369, 418, 458]. Finally, similar effects on EB1 localization, which result in microtubule co-alignment with stress fibers in cultured cells, have also been reported for members of the GAS2-like family of proteins [459, 460], which are structurally very similar to our TipAct construct.

Besides the enhanced localization of EB3 and TipAct at actin-microtubule overlaps, we also showed that the mechanical properties of the F-actin bundles *vis à vis* that of the microtubule play a key role in deciding who will guide who. *In vitro* experiments have revealed that fascin-stabilized actin bundles can reach bending stiffnesses in the range of $30 - 40$ pN µm^2 [473], depending on the number of actin filaments in the bundle. These values are well above the mechanical bending rigidity of a single microtubule (~ 8 pN µm^2 [89–91, 174]). This could help explain why in our assays, when a growing microtubule was being guided by an actin bundle, it was the microtubule which deformed. However, the F-actin bundles were also partially immobilized on the coverslip surface, which further prevented their deformation. In fact, mechanical stabilization of actin-bundles by the surrounding environment could also play a role in cells. For instance, in contrast to the fascin-stabilized actin bundles reconstituted *in vitro*, filopodial actin bundles in cells have been shown to be sparsely cross-linked structures, containing $\sim 10 - 20$ actin filaments [479–481], and a molar ratio of fascin to actin in the order of 1:25 [480]. *In vitro* measurements of F-actin bundle rigidity in these conditions would predict a bending rigidity for such bundles below 0.15 pN µm^2 [474]. This value is 50-fold lower than the bending rigidity of a single microtubule. However, in cells, filopodia do guide microtubule growth [291, 354], and furthermore have been shown to have bending rigidities in the order of 40 pN µm^2 [482]. Although the activity of additional F-actin bundlers may play a role in enhancing the mechanical stability of filopodial bundles, fascin is by far the dominant component [483]. This observation supports the notion that mechanical stabilization by the surrounding environment (i.e. the plasma membrane, the lamellipodial F-actin network, or anchoring at focal adhesions), could play a key role in providing F-actin bundles in cells with further mechanical stability in order to guide microtubule growth.

Finally, we showed that F-actin bundles, through their guiding effect on microtubule growth, can globally dictate microtubule organization. We found that both in the presence and absence of TipAct, an otherwise random array of dynamic microtubules could adopt the underlying organization of parallel arrays of F-actin bundles. However, without a direct actin-microtubule cross-linker, microtubules were susceptible to lose their F-actin track, unless the density of F-actin bundles was sufficiently high. In cells, both filopodia and stress fibers are sparse structures surrounded by crowded environments (i.e. the lamellipodial F-actin network, and the cell interior, respectively). It is thus likely that mechanical guidance by deflection is not the mechanism of choice for efficient guidance by either of these F-actin structures, which explains the need for direct actin-microtubule cross-linkers to carry out this function.

4.7 Materials and methods

4.7.1 Surface deposition of microtubule seeds and linear arrays of fascin-stabilized actin bundles

To generate parallel arrays of fascin-stabilized F-actin bundles, interspersed with a random collection of GMPCPP-stabilized microtubule seeds, we used flow cells which had entry and exit points on the glass slide side, which allowed us to sequentially flow in different solutions while monitoring the sample by TIRF microscopy (Fig. 2.2). Figure 4.14 shows the sequence of steps, and representative images of the flow-cell surface after each step.

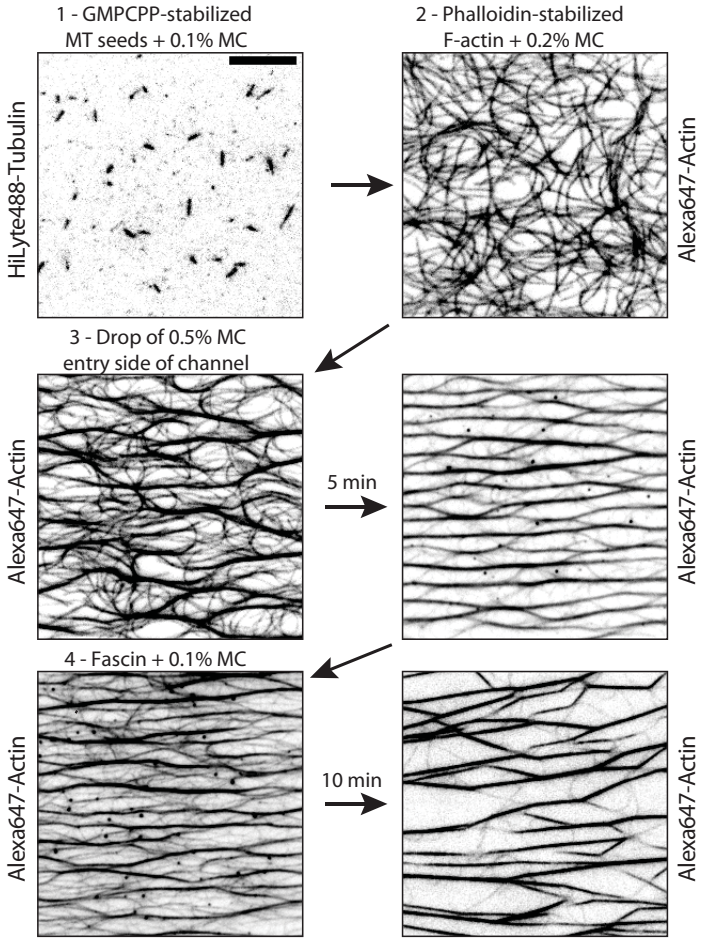

Figure 4.14: Surface deposition of microtubule seeds and linear arrays of actin bundles. TIRF images showing the sequential deposition of: (1) a random array of microtubule seeds, (2) long actin filaments, (3) a methyl-cellulose (MC) solution to align and bundle the actin filaments, and (4) a fascin solution to exchange the MC, and stabilize the F-actin bundles. Scale bar, 10 µm. MT, microtubule.

First, microtubule seeds (diluted in MRB80 with 0.1% (w/v) methyl-cellulose) were slowly added to the flow cell at what would be the equivalent of 50 - 100 nM tubulin concentration. After a 5 min incubation, the flow cell was rinsed slowly (to minimize microtubule-seed alignment) with 500 - 100 µl of MRB80. Second, pre-polymerized, phalloidin-stabilized actin filaments were added to the flow-cell at the equivalent of 1 µM G-actin concentration, in MRB80 containing 0.2% (w/v) methyl-cellulose. This was sufficient to push the filaments towards the surface without inducing bundle formation [484]. Thereafter, a drop of 0.5% (w/v) methyl-cellulose was placed at one end of the channel and allowed to diffuse in for $\sim$ 5 min to induce F-actin bundling, and cause a pressure-driven flow that aligned the bundles. After $\sim$ 5 min, the channel was rinsed with 50-100 µl of a solution containing 200-500 nM fascin, and 0.1% (w/v) methyl-cellulose. This stabilized the F-actin bundles, while removing excess methyl-cellulose. Since fascin exchanges quickly at F-actin bundles [485], its concentration in the flow-cell was kept constant for the rest of the experiment.

4.7.2 Microtubule tip-tracking assays

In all the assays shown in this chapter we aimed for long microtubules, in order to increase the chance of encounters with F-actin bundles. To this end microtubules were polymerized with 25-30 µM tubulin (always at a ratio of 1:15 labeled to unlabeled subunits), 100 nM EB3, with or without 50 nM GFP-TipAct. For experiments in which we monitored the effects of reducing TipAct concentration on the efficiency of microtubule capture by F-actin bundles, we varied the TipAct concentration between $6.5 - 50$ nM. TIRF microscopy imaging was performed between $32 - 34$°C (Table 2.1). We refer the reader to Chapter 2 for the general details on how these assays were built.

4.8 Data analysis

4.8.1 Analysis of FRAP data at growing microtubule tips and F-actin bundles

FRAP data for mCherry-EB3 and GFP-TipAct at growing microtubule plus-ends was retrieved from intensity profiles along the time-axis on kymographs of microtubule growth where either mCherry-EB3 or GFP-TipAct was bleached. Plus-ends were selected

by comparing their intensity and growth speeds to the corresponding minus-ends, and recovery was only analyzed on plus-ends that continued to grow with constant speeds after bleaching. The actual recovery data was retrieved by plotting the fluorescence intensity along a three-pixel-wide line traced vertically down the time axis on the kymograph, centered at the most intense region of the pre-FRAP plus-end intensity, to make sure that fluorescence recovery was analyzed at the same region on the microtubule lattice.

In the case of free microtubule tips (i.e. not bound to an actin bundle), and assuming that the soluble pools of mCherry-EB3 and GFP-TipAct quickly equilibrate, a reaction-limited recovery curve [486] multiplied by a decaying single-rate exponential envelope function was sufficient to describe the recovery. The decaying curve accounts for the progressive loss of affinity for EB3 at the same site on the microtubule lattice as a result of GTP hydrolysis [100]. To this curve, we added a slowly rising exponential curve shifted to $t = t_0$ in order to account for non-zero affinity of EB3 for the GDP-tubulin lattice. The equation thus used for fitting EB3 and TipAct recovery at free microtubule tips was the following:

$$\begin{aligned} I(t) = (A - B * \exp\left[-t * k_{off-free}\right]) * \\ \exp\left[-H(t-t_0) * (t-t_0) * k_{decay-free}\right] + \\ D * (1 - \exp\left[-H(t-t_0) * (t-t_0) * k_{decay-free}\right]) \end{aligned} \tag{4.1}$$

where A, B and D are constants, $k_{off-free}$ the off-rate of mCherry-EB3 (or GFP-TipAct) at microtubule tips, $k_{decay-free}$ the transition rate from a tip-like to a lattice-like binding profile (related to GTP hydrolysis), and $H(t - t_0)$ the Heaviside function to account for the fact that this transition occurs with a time delay [100]. In the case of actin-bound microtubule tips, a modified version of Eq. (4.1) was used in which two species of recovering molecules were introduced, in order to account for the fraction of mCherry-EB3 (and GFP-TipAct) molecules that were only interacting with the microtubule tip, and those linked to microtubule tip and F-actin bundle:

$$\begin{aligned} I(t) = (A - B * \exp\left[-t * k_{off-free}\right] - C * \exp\left[-t * k_{off-bound}\right]) * \\ \exp\left[-H(t-t_0) * (t-t_0) * k_{decay-bound}\right] + \\ D * (1 - \exp\left[-H(t-t_0) * (t-t_0) * k_{decay-bound}\right]) \end{aligned} \tag{4.2}$$

where A, B, C and D are constants, $k_{off-free}$ the off-rate of mCherry-EB3 (or GFP-TipAct) bound only to microtubule tips, $k_{off-bound}$ the off-rate of mCherry-EB3 (or

GFP-TipAct) bound both to the microtubule tip and actin bundle, and $k_{decay-bound}$ the transition rate from a tip-like to a lattice-like binding profile (as above). The values of $k_{off-free}$ and t_0 were fixed to the values that were obtained for free microtubule tips using Eq. (4.1). Fitting was performed on the average recovery curves (weighted by the inverse of the SEM) for n = 19 and n = 7 mCherry-EB3 and GFP-TipAct recovery profiles at free microtubule tips, and for n = 13 and n = 6 mCherry-EB3 and GFP-TipAct recovery profiles at actin-bound microtubule tips (Fig. 4.4).

FRAP data for GFP-TipAct and mCherry-EB3 on F-actin bundles and actin-microtubule lattice overlaps was similarly obtained from intensity line profiles along the time-axis on kymographs traced along the bleached F-actin bundles. Recovery data was retrieved by plotting the average fluorescence intensity along a five to ten pixel-wide line traced vertically down the time axis of the kymograph. In the case of GFP-TipAct no fitting was performed since no significant fluorescence recovery was observed (Fig. 4.5 c), at least within the same timescale of observation. On the contrary, mCherry-EB3 did exchange both on free and microtubule-bound actin bundles (Fig. 4.5 b). In the case of free actin bundles (i.e. not linked to a microtubule), and assuming that the soluble pool of mCherry-EB3 quickly equilibrates, a simple reaction-limited curve was used to describe the recovery:

$$I(t) = A - B * \exp[-t * k_{off-free}] \tag{4.3}$$

where A and B are constants, $k_{off-free1}$ the off-rate of mCherry-EB3 bound to the actin bundles via GFP-TipAct. For the case of microtubule-bound actin bundles, a modified version of Eq. (4.3) was used in which again two species of exchanging molecules were introduced, to account for the fraction of mCherry-EB3 molecules that were only interacting with the microtubule lattice, and those interacting with both microtubule lattice and TipAct at the actin bundles:

$$I(t) = A - B * \exp[-t * k_{off-free2}] - C * \exp[-t * k_{off-bound}] \tag{4.4}$$

where A, B and C are constants, $k_{off-free2}$ the off-rate of mCherry-EB3 bound only to the microtubule lattice and $k_{off-bound}$ the off-rate of mCherry-EB3 bound both to the microtubule lattice and the GFP-TipAct decorated actin bundle. Fitting was performed on the average recovery curve (weighted by the inverse of the SEM) for n = 12 curves at free actin bundles, and for n = 17 curves at microtubule-bound actin bundles (Fig. 4.5).

All fitting was performed with the *Curve Fitting Toolbox* of Matlab using the non-linear least squares method.

4.8.2 Analysis of microtubule and actin-bundle encounters

In a similar fashion to how microtubule-microtubule encounters have been classified in models of cortical microtubule arrays in plants [295], the interactions between a growing microtubule and an actin bundle were classified into three categories (Fig. 4.8 a): cross-over, catastrophe, deflection (without TipAct) and zippering (with TipAct). To quantify the probability of these outcomes, the microtubule length L_{MT} (measured from the plus end of the microtubule seed to the tip of the microtubule), and the angle θ between the orientation of the tip (defined as the end-most $\sim$2 µm-long section of microtubule) and the actin bundle, were measured at the time of intersection. Thereafter one of the outcomes defined above were assigned by monitoring the subsequent microtubule growth until the next catastrophe. This analysis was performed for n = 914, 708 interactions between growing microtubule plus-ends and F-actin bundles in the presence or absence of 50 nM GFP-TipAct, respectively, and the probability of each outcome calculated as a function of L_{MT} and θ. For the experiments with variable amounts of GFP-TipAct, the analysis was performed only for the encounter angle θ, with the exception that a new interaction outcome was included, namely *zipper & snap-off*. This analysis was performed for n = 459, 421 and 443 interactions for each of the following conditions: 6.25 nM, 12.5 nM and 25 nM GFP-TipAct, respectively.

4.8.3 Analysis of microtubule and actin bundle array orientation

To determine the orientation distributions for the linear arrays of actin bundles and the corresponding microtubule arrays, pixel-by-pixel orientation values were extracted from the fluorescence image files using the *OrientationJ* plugin [487] developed for ImageJ [443]. This plugin returns two matrices with the same size as the input image (Fig. 4.15 a), whose values at each pixel correspond to: 1) Orientation (in radians, from -$\pi/2$ to $\pi/2$), and 2) Coherency, which indicates the degree of co-alignment of a given pixel relative to its neighbors within a user-defined window (defined to range from 0 for no co-alignment, to 1 for full co-alignment). In all cases the we used the Gaussian gradient analysis method in *OrientationJ* with a window size of three pixels.

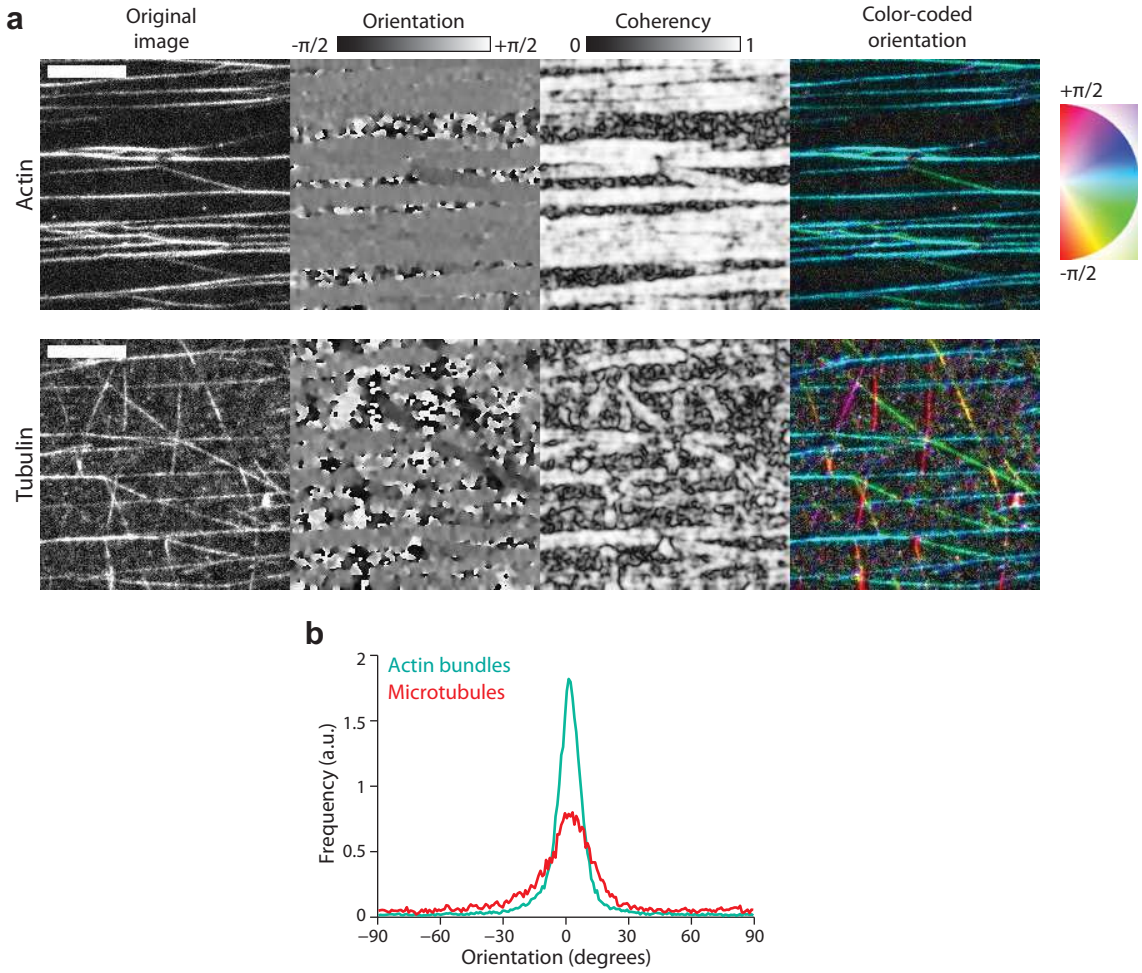

Figure 4.15: Orientation analysis. (a) Montage of the pixel-by-pixel orientation data for a sample F-actin bundle array (top), and the ensuing microtubule organization (bottom) after ~ 1 hr of growth in the presence of TipAct. The left-most panels show the fluorescence images, followed by the orientation and coherency maps. The right-most panels show the color-coded orientation maps, as indicated by the color-wheel. (b) Normalized histograms for the actin-bundle (cyan) and microtubule (red) orientations for the examples in (a). Scale bar, 10 µm.

Histograms of microtubule and actin bundle orientation angle, θ_{MT} and θ_{ACTIN} respectively (Fig. 4.15 b), were constructed using the values of the orientation matrix weighted by the coherency to minimize the contribution of pixels where no filaments were present, with a bin size of $\pi/100$. This analysis was performed for every frame in fluorescence time-lapse stacks that each corresponded to $5-10$ minutes of microtubule growth. These histograms were averaged over two minutes of microtubule growth (60 frames) and with these average curves the time-evolution of the distribution of θ_{MT} and the average distribution of θ_{ACTIN} were built (Fig. 4.10). Time zero was defined as the point when the first stack of fluorescence images was recorded; which was typically

$\sim 2-3$ min after the microtubule polymerization mix was added to the flow cell channel.

The same distributions of microtubule orientation angle (θ_{MT}), averaged over two minutes of microtubule growth, were used to build the average orientation distribution for all microtubule alignment experiments (Fig. 4.12), both with and without GFP-TipAct, for the cases where the average microtubule length was short ($\langle L_{MT} \rangle \leq 19$ µm) and long ($\langle L_{MT} \rangle > 19$ µm), as defined in Figure 4.11. To this end, all the orientation histograms corresponding to short and long microtubules were collected and shifted along the x-axis such that their corresponding mean actin orientation angle ($\langle \theta_{ACTIN} \rangle$) would fall at 0°. Thereafter, the curves were averaged and the resulting histogram was fit with the *Curve Fitting Toolbox* of Matlab using the non-linear least squares method to a Gaussian function of the form:

$$y(\theta) = A \exp\left(\frac{-(\theta - \mu)^2}{2\sigma^2}\right) + B \tag{4.5}$$

where, A is a constant, μ the mean location, σ the standard deviation, and B an offset due to noise. The value of μ represents the difference in mean orientation between the microtubules and the actin bundle array, i.e. $\langle \theta_{ACTIN} \rangle - \theta_{MT}$, which can be understood as the *centering efficiency*, the smaller its value, the better the actin-microtubule co-alignment. On the other hand, the value of σ can be interpreted as the *focusing efficiency*, that is, the smaller its value, the more globally the microtubule array has been aligned by the underlying actin bundle array. We performed this analysis for n = 6 experiments with GFP-TipAct, comprising n= 17 histograms for long microtubules and 18 histograms for short microtubules; and for n = 9 experiments without GFP-TipAct comprising 9 histograms for long microtubules and 11 histograms for short microtubules.

4.8.4 Analysis of average microtubule length

Microtubule lengths were measured manually by tracing lines along the microtubules using the *Segmented Line* function in FIJI [442]. This was performed approximately every $6-10$ min for a $\sim$50 min experiment in conditions where the average microtubule length ($\langle L_{MT} \rangle$) continuously increased, as was the case for all the experiments with linear arrays of actin bundles performed in this chapter. With these values, histograms of microtubule length were constructed with a bin size of 5 µm (Fig. 4.16 a), and fitted with a simple Exponential or Gaussian function (depending on a qualitative assessment

of the shape of the histogram), to obtain a value for the average microtubule length $\langle L_{MT} \rangle$. These values were used to construct a plot of $\langle L_{MT} \rangle$ over time (Fig. 4.16 b).

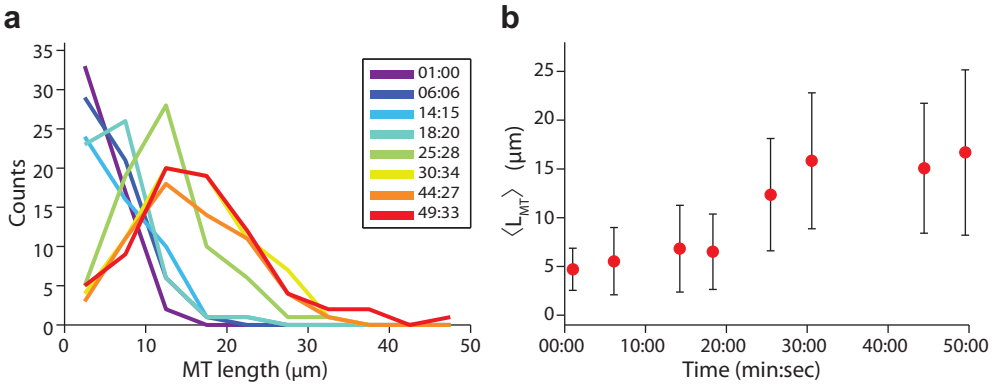

Figure 4.16: Analysis of $\langle L_{MT} \rangle$ over time. (a) Time-evolution of microtubule-length distribution for a 50 min-long dynamic microtubule experiment with the same growth conditions as the experiments with arrays of actin bundles (Fig. 4.10). The color-code indicates time as displayed in the legend (min:sec). (b), Increase in average microtubule length $\langle L_{MT} \rangle$ with time. Data points show the average of the distributions obtained by fitting an Exponential (for $t < 20$ min) or a Gaussian (for $t \geq 20$ min) distribution to the histograms in (a). Error bars indicate STD.

4.8.5 Analysis of microtubule and actin surface coverage, and actin-microtubule overlap

In order to analyze the area fraction covered by microtubules, as well as the extent of actin-microtubule overlap, binary masks were generated for both microtubule and F-actin bundle arrays using custom-written programs based on the *Image Processing Toolbox* of Matlab (Fig. 4.17 b). These masks were generated through a combination of adaptive thresholding and morphological operations.

The area coverage was defined as the ratio of the total number of white pixels in the microtubule (or F-actin) mask divided by the total number of pixels in the image (i.e. 512×512), a number which by definition ranges from zero to one. Similarly, the degree of microtubule overlap with F-actin was defined as the total number of white pixels common to the actin and microtubule masks (i.e. overlapping mask pixels, Fig. 4.17 b), divided by the total number of white pixels in the microtubule mask. By definition, this value also ranges from zero to one. The decision to use overlap instead of colocalization analysis was based on two reasons: first, because the tubulin channel was often noisy since the levels of fluorescent tubulin were kept low; and second, because we were

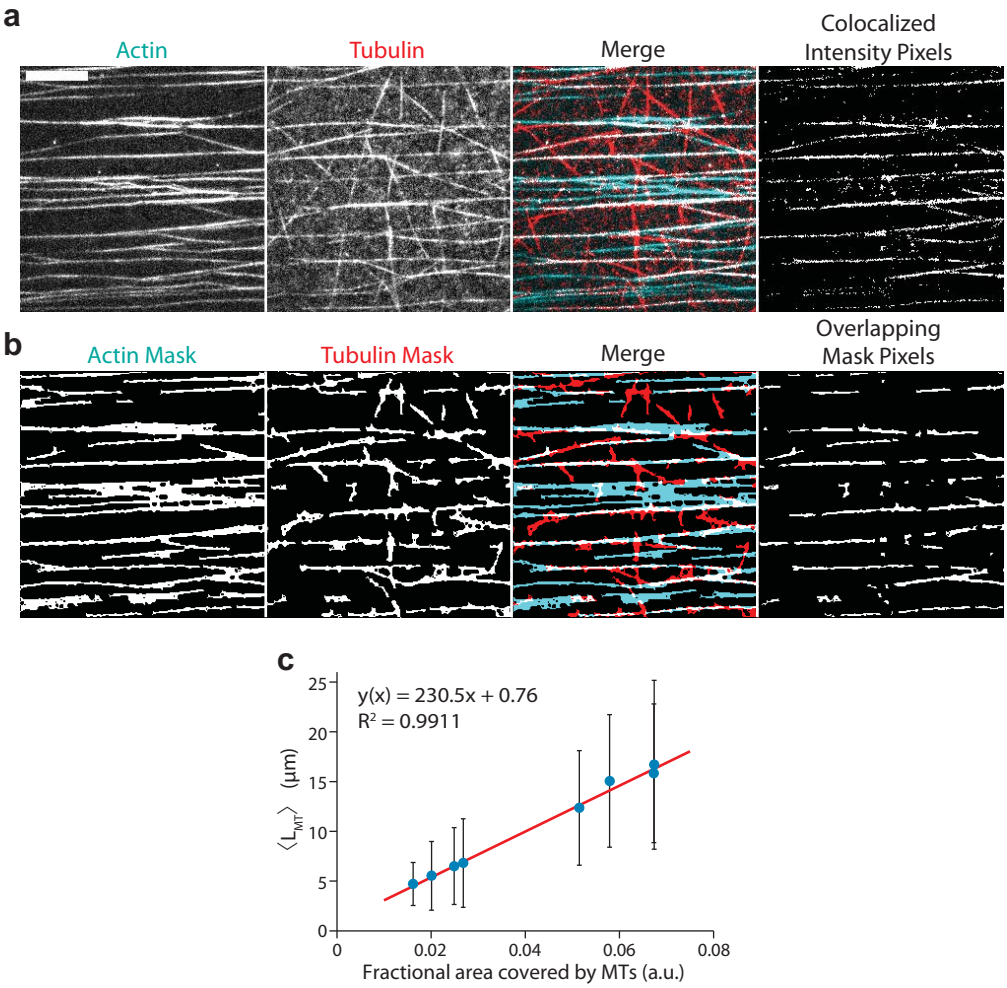

Figure 4.17: Co-localization *versus* overlap analysis, and relationship between $\langle L_{MT} \rangle$ and actin-microtubule overlap. (a) Example of co-localization analysis for the same experiment as in Figure 4.15. The two left-most panels show the actin and tubulin fluorescence intensity images, and the third panel the merged image. The right-most panel shows the co-localized intensity pixels as produced by the *Colocalization Threshold* plugin in FIJI, which estimated that 47% of the microtubule signal overlapped with that of the actin. (b) Example of area coverage and overlap analysis for the same F-actin bundle and microtubule arrays as in (a). The two left-most panels show the binary masks generated from the intensity data. The third panel shows the merged image of the binary masks, with the same color-code as in (a). The right-most panel shows the pixels that are common to both masks, i.e. the overlap between the F-actin bundles and the microtubules (48% of the pixels), which is to be compared with the co-localized intensity pixel panel in (a). (c) Linear relationship between the average microtubule length $\langle L_{MT} \rangle$, and the fraction of the image area covered by microtubules, for the same experiment as in Figure 4.16. Scale bars, 10 µm.

not interested in the correlation between the tubulin and actin intensities, but rather, within the limits of optical resolution, whether microtubules co-localized with the F-actin bundles or not. For this purpose, a binary measure was sufficient. Figure 4.17 shows a comparison between co-localization and overlap analysis that validates this approach. Panel a shows the individual intensity images, followed by the merged image and the percentage of co-localized signal as estimated using the *Colocalization Threshold* plugin in FIJI [442], which estimated that 47% of the tubulin signal colocalized with that of the actin. Conversely, panel b in Figure 4.17 shows the results of a custom-written overlap analysis program for the same images; the first two panels show the binary intensity masks generated as previously explained, the third panel the combined masks where the white pixels are those common to both masks (i.e. the overlap), which are shown alone in the last panel. In this case, 48% of the white pixels in the microtubule mask were also present in the actin mask, which is in good agreement with the estimation of the percent of colocalized signal mentioned above. Finally, as can be observed in Figure 4.17, conservative settings were used to create the binary masks so that, if anything, the actual degree of actin-microtubule overlap was underestimated. Masks were obtained for every tenth image in a stack (that is every 20 s of microtubule growth) for stacks that corresponded to five to ten minutes of microtubule growth.

4.8.6 Estimating the relationship between the area covered by microtubules and the average microtubule length

The fraction of the field of view covered by microtubules was used as a proxy for their average length $\langle L_{MT} \rangle$, since in the conditions of the co-alignment experiments microtubules grew progressively longer and the surface crowded (Fig. 4.10), making it difficult to measure microtubule lengths individually. This approach was validated by tracking the distribution of microtubule lengths over time for an experiment that evolved from short to long microtubules (Fig. 4.16) and by plotting the obtained values for $\langle L_{MT} \rangle$ against the fraction of the area covered by the microtubules at the same time-point (as obtained from the binary masks). As can be observed in panel c of Figure 4.17 these values were linearly related. The parameters of the best linear fit through the data points were thus used to get an estimate of $\langle L_{MT} \rangle$ for all experiments analyzed in Figure 4.11. It is worth noting that since this approximation only holds for fields of view with approximately equal numbers of microtubule seeds, the only experiments analyzed were those in which there were $\sim 50 \pm 10$ microtubule seeds in the field of view.

4.8.7 Determination of global F-actin bundle and microtubule alignment

The pixel-by-pixel orientation and coherency values that were used to build histograms of actin-bundle and microtubule orientation (Fig. 4.15) were also used to estimate the degree of actin bundle and microtubule alignment. This was performed with the use of an order parameter (OP), a unit-less quantity that conveys the degree of alignment of filamentous structures independent of filament polarity [477]. In two dimensions, the OP can be defined as follows:

$$OP = \left[\left(\frac{\sum_{i=1}^{n} w_i \cos(2\theta_i)}{\sum_{i=1}^{n} w_i} \right)^2 + \left(\frac{\sum_{i=1}^{n} w_i \sin(2\theta_i)}{\sum_{i=1}^{n} w_i} \right)^2 \right] \tag{4.6}$$

where θ_i and w_i correspond to the i$^{\text{th}}$ pixel's orientation and coherency values, and n to the number of pixels in the image (i.e. 512×512). By definition the OP ranges from zero (when all values of θ_i are randomly distributed) to one (in which all values of θ_i are the same).

4.8.8 Criteria for comparing experiments with linear arrays of actin bundles

A strategy had to be devised in order to fairly compare experiments of actin-microtubule co-alignment (Figures 4.11 ad 4.12), in order to make sure that the actin-bundle arrays were similarly ordered and spaced; as well as to ensure that microtubule growth started from an isotropic collection of microtubule seed orientations. To this end, experiments were compared if the microtubule seed array had an $OP \leq 0.2$, with $\sim 50 \pm 10$ microtubule seeds in the field of view. For the linear arrays of F-actin bundles, experiments were included in the analysis of Figure 4.11 if the arrays had an $OP \geq 0.80$. Since the number of bundles in the field of view could not be precisely counted, the fraction of the field of view covered by the actin bundles (as explained above) was used as a proxy for the number of bundles, and the analysis was limited to actin-bundle arrays with area coverage between 0.1-0.25.

4.8.9 Evolution of order parameter and actin-microtubule overlap as a function of the average microtubule length $\langle L_{MT} \rangle$

To build plots of microtubule alignment and actin-microtubule overlap versus $\langle L_{MT} \rangle$ (Figures 4.11 ad 4.12), these values were obtained for every tenth image in a stack (that is every 20 s of microtubule growth) and averaged over five-minutes of microtubule growth. The mean ± standard deviation of these values was then plotted for all fluorescence stacks across comparable experiments. This was performed for n = 6 experiments with GFP-TipAct comprising n = 20 different actin bundle arrays; and for n = 26 experiments without GFP-TipAct comprising n = 26 different actin bundle arrays. This means that the points in Figure 4.11 do not all represent different experiments but rather, the average of five minutes of microtubule growth within various actin bundle arrays that were collected over various experiments.

We would like to thank Florian Huber (FOM Institute AMOLF, The Netherlands) for advice on the generation of parallel arrays of actin bundles, and Feng-Ching Tsai (FOM Institute AMOLF) for help with the fascin purification. We also thank Bela Mulder (FOM Institute AMOLF) for his advice on the analysis of the orientation and order parameter of actin and microtubule arrays.